



Joint inversion for V_p, V_s, and V_p/V_s at SAFOD, Parkfield, California

Haijiang Zhang

Department of Earth, Atmospheric, and Planetary Sciences, Massachusetts Institute of Technology, Cambridge, Massachusetts 02139, USA (hjzhang@mit.edu)

Also at Department of Geoscience, University of Wisconsin–Madison, Madison, Wisconsin 53706, USA

Clifford Thurber

Department of Geoscience, University of Wisconsin–Madison, Madison, Wisconsin 53706, USA

Paul Bedrosian

U.S. Geological Survey, Denver, Colorado 80225, USA

[1] We refined the three-dimensional (3-D) V_p, V_s and V_p/V_s models around the San Andreas Fault Observatory at Depth (SAFOD) site using a new double-difference (DD) seismic tomography code (tomoDDPS) that simultaneously solves for earthquake locations and all three velocity models using both absolute and differential P, S, and S-P times. This new method is able to provide a more robust V_p/V_s model than that from the original DD tomography code (tomoDD), obtained simply by dividing V_p by V_s. For the new inversion, waveform cross-correlation times for earthquakes from 2001 to 2002 were also used, in addition to arrival times from earthquakes and explosions in the region. The V_p values extracted from the model along the SAFOD trajectory match well with the borehole log data, providing in situ confirmation of our results. Similar to previous tomographic studies, the 3-D structure around Parkfield is dominated by the velocity contrast across the San Andreas Fault (SAF). In both the V_p and V_s models, there is a clear low-velocity zone as deep as 7 km along the SAF trace, compatible with the findings from fault zone guided waves. There is a high V_p/V_s anomaly zone on the southwest side of the SAF trace that is about 1–2 km wide and extends as deep as 4 km, which is interpreted to be due to fluids and fractures in the package of sedimentary rocks abutting the Salinian basement rock to the southwest. The relocated earthquakes align beneath the northeast edge of this high V_p/V_s zone. We carried out a 2-D correlation analysis for an existing resistivity model and the corresponding profiles through our model, yielding a classification that distinguishes several major lithologies.

Components: 8910 words, 11 figures.

Keywords: SAFOD; V_p; V_s; V_p/V_s; resistivity.

Index Terms: 7270 Seismology: Tomography (6982, 8180).

Received 30 June 2009; **Revised** 8 September 2009; **Accepted** 17 September 2009; **Published** 5 November 2009.

Zhang, H., C. Thurber, and P. Bedrosian (2009), Joint inversion for V_p, V_s, and V_p/V_s at SAFOD, Parkfield, California, *Geochem. Geophys. Geosyst.*, 10, Q11002, doi:10.1029/2009GC002709.

1. Introduction

[2] In summer 2007, the San Andreas Fault Observatory at Depth (SAFOD) penetrated the San Andreas fault (SAF) at seismogenic depths with the goal of addressing fundamental questions regarding earthquakes and fault mechanics [Zoback *et al.*, 2007]. The SAFOD site is located near Parkfield, California, 1.8 km southwest of the SAF surface trace (Figure 1). Here the SAF separates two distinct geologic terrains, with the Salinian block to the southwest of the fault and Franciscan mélangé unconformably overlain by unmetamorphosed sedimentary rocks of the Great Valley sequence to the northeast. The Salinian block mainly consists of granitic rocks and the Franciscan mélangé is composed of greywacke, greenstone, chert, serpentinite, and blueschist [Page, 1981].

[3] The geophysical properties of the crust around the Parkfield region and at the SAFOD site have been characterized by a number of previous studies, including studies of seismic velocity [Lees and Malin, 1990; Ben-Zion and Malin, 1991; Michelini and McEvilly, 1991; Eberhart-Phillips and Michael, 1993; Thurber *et al.*, 2003, 2004; Roecker *et al.*, 2004, 2006; Zhang and Thurber, 2005; Hole *et al.*, 2006; Malin *et al.*, 2006; Bleibinhaus *et al.*, 2007], seismic attenuation [Abercrombie, 2000; Bennington *et al.*, 2008], seismic anisotropy [Boness and Zoback, 2006; Zhang *et al.*, 2007; Liu *et al.*, 2008], electrical resistivity [Unsworth *et al.*, 1997, 2000; Unsworth and Bedrosian, 2004; Becken *et al.*, 2008], and potential fields [McPhee *et al.*, 2004]. All the seismic velocity studies reported a velocity contrast across the SAF, faster to the southwest and slower to the northeast. Similarly, the electrical resistivity studies showed generally higher resistivity to the southwest of the fault compared to the northeast side, along with a very low resistivity zone adjacent to the SAF trace on the southwest side.

[4] The SAFOD borehole trajectory was guided by high-precision earthquake relocation efforts by several groups, including location and tomography results from Thurber *et al.* [2003, 2004, 2006] and Zhang and Thurber [2005]. Although nearly all of the seismic stations used in these studies were three-component, interpretation of the Vs or Vp/Vs models and their comparison to the Vp model were hampered by the poorer resolution of the former models compared to the Vp model, as is commonly the case [Eberhart-Phillips, 1990]. In this study, an abundance of P wave data from

explosions is the main reason for the resolution differences.

[5] We present new three-dimensional (3-D) Vp, Vs, and Vp/Vs models around the SAFOD site that are obtained using a new double-difference seismic tomography code (tomoDDPS). The new algorithm is able to solve simultaneously for Vp, Vs, Vp/Vs, and event locations using both absolute and differential P, S, and S-P times. This strategy avoids the pitfalls of using, for example, Vp and Vs models to infer Vp/Vs via division, and is able to produce a reliable Vp/Vs model. In addition to Vp and Vs models, knowing 3-D Vp/Vs (or Poisson's ratio) variations is helpful for having a more complete characterization of the mechanical properties and geological strata. Compared to most previous models, the grid spacing for the new model is finer, with a horizontal grid interval of 0.7 to 3 km. Also, differential times derived from waveform cross correlation were used in this study, while only catalog differential times were used in the previous DD tomography study of Zhang and Thurber [2005] for the same region. The new 3-D velocity models are helpful for better understanding the detailed structure around SAFOD and its relationship with local seismicity. We also conduct a 2-D correlation analysis of the Vp, Vs and Vp/Vs models with an existing resistivity model along the same profile through the SAFOD site. The correlation analysis is able to classify several major lithologies around SAFOD.

2. Data

[6] We use a data set similar to that of Thurber *et al.* [2004] and Zhang and Thurber [2005], with some additional earthquake and explosion data obtained when temporary surface and borehole instruments were deployed from 2004 to 2006. Figure 2 shows a map of the events and stations used in this study. The main source of data is a temporary seismic array known as the Parkfield Area Seismic Observatory (PASO) [Thurber *et al.*, 2003, 2004]. All of the PASO array stations have three-component sensors with the majority of them being broadband. We also include data from the UC-Berkeley High Resolution Seismic Network (HRSN), fault zone guided wavefield projects in 1994 [Li *et al.*, 1997] and 2004 [Li and Malin, 2008], the USGS Central California Seismic Network, and USGS temporary stations. Earthquake and explosion data were also obtained from borehole seismic strings deployed in the SAFOD Pilot Hole in July 2002 [Chavarria *et al.*, 2003] and in

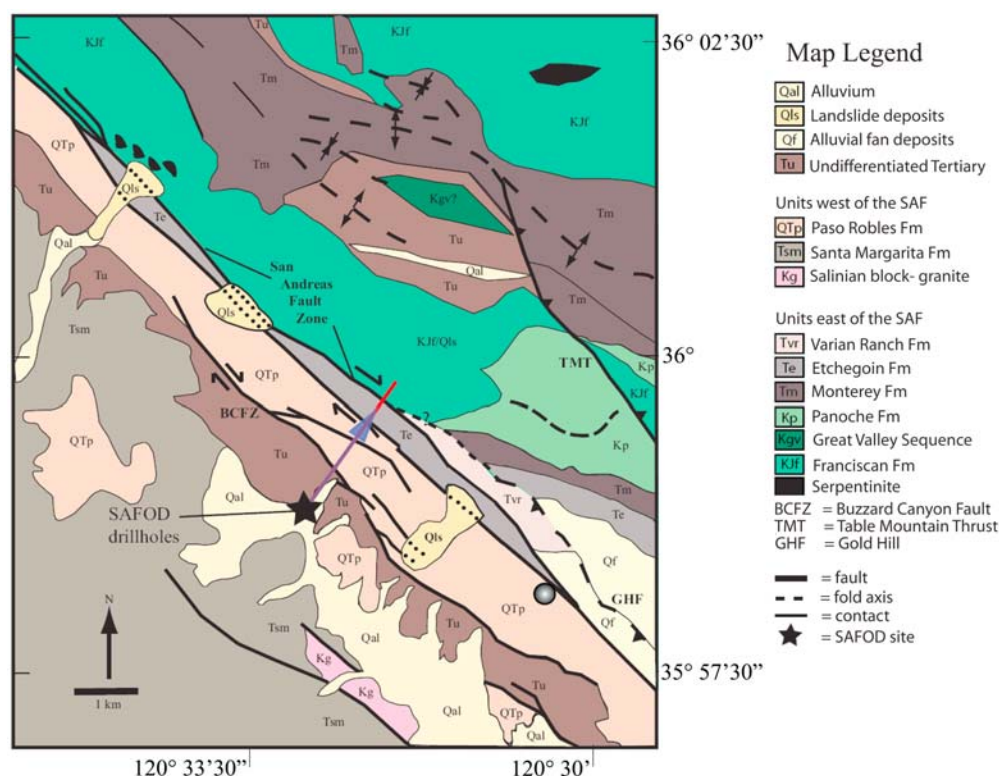


Figure 1. Geologic map of the area around the SAFOD site (modified from *Bradbury et al.* [2007]).

the SAFOD main borehole in May 2005 by Paulsson Geophysical Services, Inc., as well as from borehole geophones deployed periodically in the SAFOD borehole between December 2004 and November 2006 by the SAFOD project. Sources of explosion data include a ~ 5 km long high-resolution reflection/refraction line in 1998 [*Hole et al.*, 2001; *Catchings et al.*, 2002], a ~ 50 km long reflection/refraction line in 2003 [*Hole et al.*, 2006], and PASO “calibration” shots in 2002, 2003, 2004, and 2006. In total, there are 1563 events including 574 earthquakes, 836 shots (explosions with known location and origin times), and 153 blasts (explosions with known location and uncertain origin times). There are about 90,800 arrival times (72% P and 28% S) included in the joint inversion for earthquake locations and 3-D velocity structure. For the 574 earthquakes, differential times (approximately 489,000 P and 364,000 S) from event pairs observed at common stations were also calculated using a waveform cross-correlation package BCSEIS [*Du et al.*, 2004].

3. Methodology

[7] *Zhang and Thurber* [2003] developed a double-difference (DD) seismic tomography method that

makes use of both absolute arrival times and more accurate differential times. It simultaneously solves for the 3-D velocity structure (V_p and V_s) and seismic event locations. In terms of characterizing

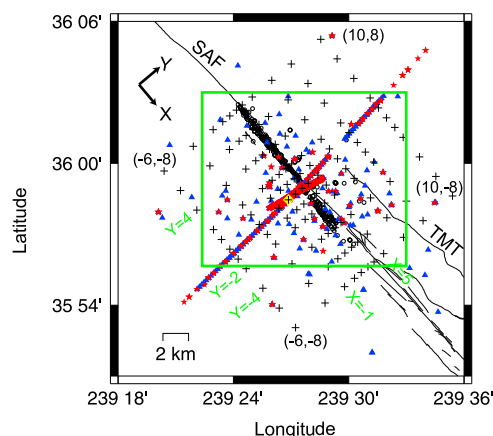


Figure 2. Map of seismicity (black dots), seismic stations (blue triangles), shots (red stars), faults (black lines), and inversion grid nodes (black crosses). Yellow square indicates the SAFOD site and the Cartesian coordinate center. The inversion grid nodes are located at $X = -6, -3, -1, 0, 0.7, 1.4, 2.0, 3.0, 5.0, 7.0,$ and 10.0 km and $Y = -8, -6, -4, -2, -1, 0, 1, 2, 4, 6,$ and 8 km. Green box approximately delineates the area shown in Figure 1. SAF, San Andreas Fault; TMT, Table Mountain Thrust.



the mechanical and geological properties of crustal materials, however, knowledge of 3-D Vp/Vs is of primary importance because of its direct relationship with Poisson's ratio [Eberhart-Phillips, 1990; Thurber, 1993]. The Poisson's ratio for most materials is between 0.0 and 0.5, but falls in a narrow range for crustal rocks, for example ~ 0.2 for sandstones, ~ 0.3 for carbonate rocks, $0.2\sim 0.3$ for granite, and above 0.3 for shale [Christensen, 1996]. Poisson's ratio is a useful indicator of lithology and pore fluid pressure since it depends strongly on the overall volume of cracks and their aspect ratios [Koch, 1992]. Accurate Vp/Vs variations can be determined directly from the Vp and Vs models if they have essentially identical quality. In cases where S wave arrival data are less numerous and/or of poorer quality than P wave data, however, Vs will not be as well resolved as Vp, making the interpretation of Vp/Vs variations difficult [Eberhart-Phillips, 1990]. Alternatively, Vp/Vs variations can be determined by the inversion of S-P time differences [Walck, 1988; Thurber, 1993]. By assuming that the raypaths of P and S waves are identical, which is true when Vp/Vs is constant, Vp/Vs can be related to S-P arrival time differences, $T_s - T_p$, as follows [Thurber, 1993],

$$T_s - T_p = \int_{\text{path}} \left(\frac{V_p}{V_s} - 1 \right) \frac{d\ell}{V_p} \quad (1)$$

where T_s and T_p are S and P wave arrival times at one station and $d\ell$ is an element of path length. Note that S and P waves from the same event share the same origin time, thus the unknown origin times are removed from this equation. In this algorithm, the Vp and Vp/Vs ratio models are determined using P and S-P times. After each iteration, new Vs values are calculated using the updated Vp values and Vp/Vs ratios in order to allow the calculation of the S wave raypaths in the next iteration.

[8] The above algorithm suffers two potential problems: (1) In the case of complex 3-D structure, some P and S raypaths may differ significantly and thus the results may be biased when equation (1) is applied to them and (2) the Vs structure cannot be inferred reliably from Vp and Vp/Vs values [Wagner et al., 2005], similar to the problem of inferring Vp/Vs from Vp and Vs [Eberhart-Phillips, 1990]. To reduce the effect of the assumption of similar raypaths for P and S waves, we use two strategies in our inversion algorithm: (1) At each iteration, we check P and S raypaths and remove the corresponding S-P time from the Vp/Vs inversion if the

paths differ by more than a specified threshold and (2) we use the differential S-P times from event pairs at common stations in the same way as DD tomography [Zhang and Thurber, 2003] to determine the Vp/Vs ratio in the source region [Zhang, 2003]. For strategy 2, by using the differential S-P times, we can remove the effect of different raypaths of P and S waves outside the source region, as the P and S wave raypaths are generally quite close to each other near the source. We do not obtain the Vs model using Vp values and Vp/Vs ratios since this method may result in biased Vs values [Eberhart-Phillips, 1990; Wagner et al., 2005]. Instead, we use S arrival times to solve directly for the Vs model. Thus our system simultaneously includes P, S and S-P times.

[9] Based on equation (1), the differential S-P arrival time residuals from event i to station k can be linearly related to the perturbations of event locations and Vp/Vs ratios, as follows,

$$\begin{aligned} dr_{kSP}^i &= (T_{ks}^i - T_{kp}^i)^{\text{obs}} - (T_{ks}^i - T_{kp}^i)^{\text{cal}} \\ &= \sum_{l=1}^3 \frac{\partial T_{ks}^i}{\partial x_l^i} \Delta x_l^i - \sum_{l=1}^3 \frac{\partial T_{kp}^i}{\partial x_l^i} \Delta x_l^i + \int_i^k \delta(Vp/Vs)^{d\ell}/v_p \end{aligned} \quad (2)$$

where $(T_s - T_p)^{\text{cal}}$ is the calculated differential time between the S and P wave arrival time at a given station, $(T_s - T_p)^{\text{obs}}$ is the observed differential time, and $\delta(Vp/Vs)$ is the perturbation to Vp/Vs [Zhang, 2003]. Similar to the equations of DD tomography, we subtract an equivalent equation for event j observed at station k from equation (2), as follows,

$$\begin{aligned} dr_{kSP}^{ij} &= dr_{kSP}^i - dr_{kSP}^j \\ &= \sum_{l=1}^3 \left(\frac{\partial T_{ks}^i}{\partial x_l^i} - \frac{\partial T_{kp}^i}{\partial x_l^i} \right) \Delta x_l^i - \sum_{l=1}^3 \left(\frac{\partial T_{ks}^j}{\partial x_l^j} - \frac{\partial T_{kp}^j}{\partial x_l^j} \right) \Delta x_l^j \\ &\quad + \int_i^k \delta(Vp/Vs)^{d\ell}/v_p - \int_j^k \delta(Vp/Vs)^{d\ell}/v_p \end{aligned} \quad (3)$$

where

$$\begin{aligned} dr_{kSP}^{ij} &= (T_{ks}^i - T_{kp}^i)^{\text{obs}} - (T_{ks}^i - T_{kp}^i)^{\text{cal}} - (T_{ks}^j - T_{kp}^j)^{\text{obs}} \\ &\quad + (T_{ks}^j - T_{kp}^j)^{\text{cal}} = (T_{ks}^i - T_{ks}^j)^{\text{obs}} - (T_{kp}^i - T_{kp}^j)^{\text{obs}} \\ &\quad - (T_{ks}^i - T_{ks}^j)^{\text{cal}} + (T_{kp}^i - T_{kp}^j)^{\text{cal}} \end{aligned} \quad (4)$$

Equation (3) shows that we can image the Vp/Vs structure directly using the differential P and S arrival times. These differential times can be

determined from waveform cross-correlation techniques for similar waveforms or directly from the absolute catalog data.

[10] We combine the DD tomography equations for P and S wave data and equations (2) and (3) for absolute and differential S-P data, respectively, to solve for event locations, V_p , V_s , and V_p/V_s models. We note that the generally greater accuracy of the differential data and the enhanced ability to detect and automatically down-weight outliers make the DD approach so powerful. Similar to the smoothing constraints applied to velocity changes during the inversion [Zhang and Thurber, 2003], we also apply smoothing constraints to the perturbations to V_p/V_s during each step of the joint inversion. The smoothing weights applied to the perturbations of V_p/V_s are smaller than the weights for V_p and V_s changes due to the smaller magnitude of V_p/V_s values and derivatives. The relative weightings between the different data types are treated in the same manner as in DD tomography, using a progressive strategy [Zhang and Thurber, 2003]. The absolute catalog data are weighted heavily first to determine the larger-scale structure and preliminary event locations. Then the differential data (both catalog and waveform cross correlation) are weighted heavily to further refine the velocity models and event locations. S-P data are assigned the same weights as the corresponding S wave data.

4. Inversion Details and Model Resolution Analysis

[11] For the inversion, the Cartesian coordinate center is located at the SAFOD main hole and the y axis rotated 40° counterclockwise from north so that it is parallel to the local strike of the SAF. The x axis is oriented positive northeast and the Z axis is oriented positive downward. The inversion grid nodes are located at $X = -6, -3, -1, 0, 0.7, 1.4, 2.0, 3.0, 5.0, 7.0$, and 10.0 km, $Y = -8, -6, -4, -2, -1, 0, 1, 2, 4, 6$, and 8 km, and $Z = -0.5, 0.0, 0.5, 1.0, 2.0, 4.0, 7.0$, and 10 km. Based on previous tomography results [e.g., Thurber *et al.*, 2003], we start the inversion from a two-dimensional (2-D) velocity model that incorporates a velocity contrast across the SAF, with the southwest side ranging from 0.3 to 1.1 km/s faster from the surface to 7 km depth for faster solution convergence and a constant V_p/V_s value of 1.75. We also tested the case of reducing the velocity contrast by 50% and the final velocity models are comparable to the previous ones. In the extreme

case of no velocity contrast at all in the starting model, the solution still converges and the final models are similar to other models. These tests indicate that our models are robust and are not dependent on starting velocity models.

[12] The initial root-mean-square (RMS) residuals for absolute P, S, and S-P times for the 2-D starting model are 116, 232, and 214 ms, and after the inversion, they decrease to 43, 89, and 86 ms, respectively. The initial RMS residuals for catalog differential P, S, and S-P times are 58, 85, and 85 ms and they decrease to 35, 51, and 74 ms in the final inversion, respectively. In comparison, the RMS residuals for cross-correlation P, S, and S-P times drop from 52, 115, and 41 ms initially to final values of 11, 13, and 13 ms, respectively.

[13] We first use the derivative weigh sum (DWS) distribution to assess the model quality. The DWS is a statistical parameter that helps the assessment of parameter resolution; it gives a measure of density of rays that pass near a grid point that is weighted according to how close each ray passes to the node [Toomey and Foulger, 1989]. It is, therefore, superior to the more commonly quoted “hit” matrix, which is merely a count of the number of rays that pass close to the grid point. Figure 3a shows the P and S wave DWS distributions for the combination of absolute times, differential catalog times, and cross correlation times. It can be seen that at shallow depths the P wave DWS values are generally greater than the S wave DWS values, especially for the cross sections of $Y = 0, -2$ and -4 km. This is mainly due to the large amount of shot and blast data used in this study. Therefore, it is expected that the V_p model is better resolved at shallow depths than the V_s model. In the middle part of the model, i.e., between $X = -4$ and 6 km, both P and S wave DWS distributions are relatively good, indicating that this part of the model can be resolved.

[14] However, like the ray hit count, the DWS also does not take into account the ray direction. To assess the raypath angular coverage, we calculate the mean resultant length \bar{R} of ray vectors for each inversion grid node [Fisher, 1995]. Assuming there are n rays around one inversion grid node and the direction cosines of the i th ray are a_i , b_i , and c_i , the mean resultant length \bar{R} is calculated as

$$\bar{R} = \sqrt{\left(\sum_{i=1}^n a_i\right)^2 + \left(\sum_{i=1}^n b_i\right)^2 + \left(\sum_{i=1}^n c_i\right)^2} / n \quad (5)$$

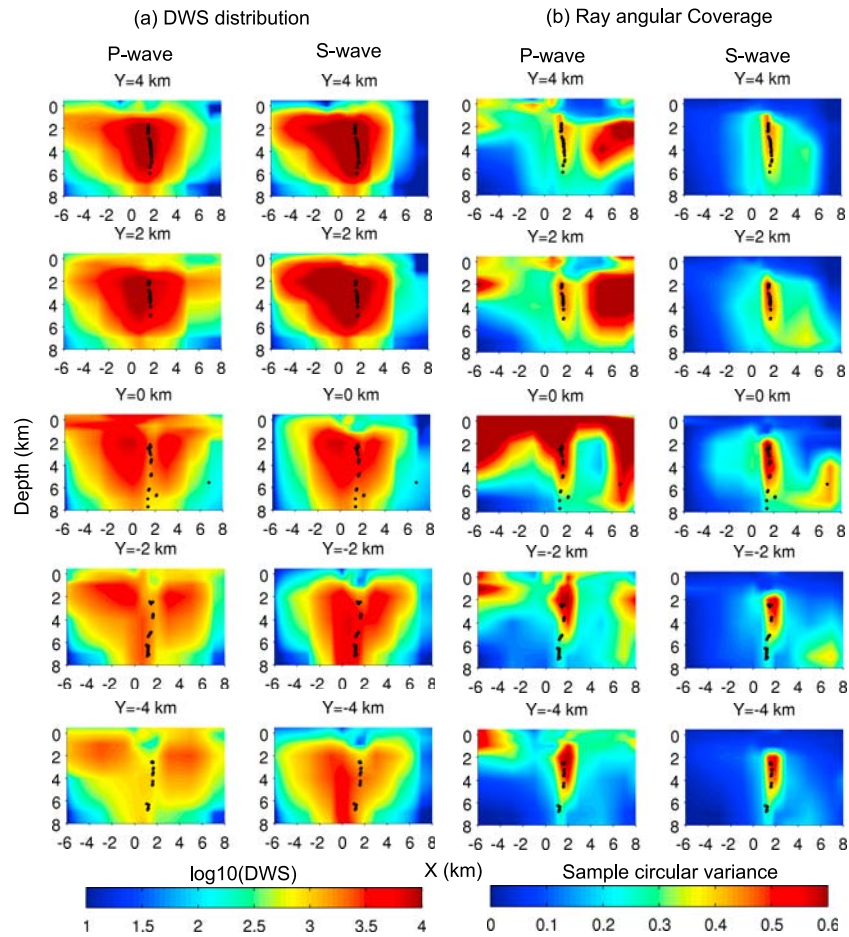


Figure 3. (a) DWS distribution and (b) ray angular coverage indicated by sample circular variance for P and S waves for across-fault cross sections at $Y = 4, 2, 0, -2$, and -4 km.

The mean resultant length \bar{R} lies in the range $[0, 1]$ and $\bar{R} = 1$ implies all rays are coincident. However, $\bar{R} = 0$ does not necessarily imply uniform dispersion [Fisher, 1995]. The quantity $V = 1 - \bar{R}$ is defined as the sample circular variance and generally the smaller the value of the circular variance, the more concentrated the ray coverage [Fisher, 1995]. Figure 3b shows the P and S wave circular variances for different across-fault cross sections at $Y = 4, 2, 0, -2$ and -4 km. To calculate circular variances for each node, only absolute raypaths are used. It can be seen that around the seismic source region, the rays are more dispersed. This is expected because the seismic events are mostly concentrated along a plane. The raypath coverage for P wave is more dispersed than the S wave ray coverage, indicating that the V_p model has better resolution than the V_s model.

[15] We also computed the resolution matrix of the inverse problem using the Partial Reorthogonalization Package (PROPACK) developed by Larsen

[1998] (the PROPACK package realizing this algorithm is available at <http://soi.stanford.edu/~rmunk/PROPACK/>, last updated on 20 April 2005). PROPACK has the ability to efficiently and accurately estimate singular values and vectors for large matrices based on the Lanczos bidiagonalization with partial reorthogonalization. Following the work of incorporating the PROPACK package into tomoDD [Zhang and Thurber, 2007], we also combined tomoDDPS with PROPACK to estimate resolution matrix for V_p , V_s and V_p/V_s parameters. Figure 4 shows diagonal resolution matrix values of V_p , V_s , and V_p/V_s for different across-fault cross sections at $Y = 4, 2, 0, -2$ and -4 km. As suggested from the DWS and circular variance distribution, the V_p model is better resolved than the V_s model, especially at shallow depths. The V_p/V_s model has a very similar resolution distribution as the V_s model because the S-P data distribution is similar to the S data distribution. As stated by Zhang and Thurber [2007], the DWS distribution is a good indicator of the resolution

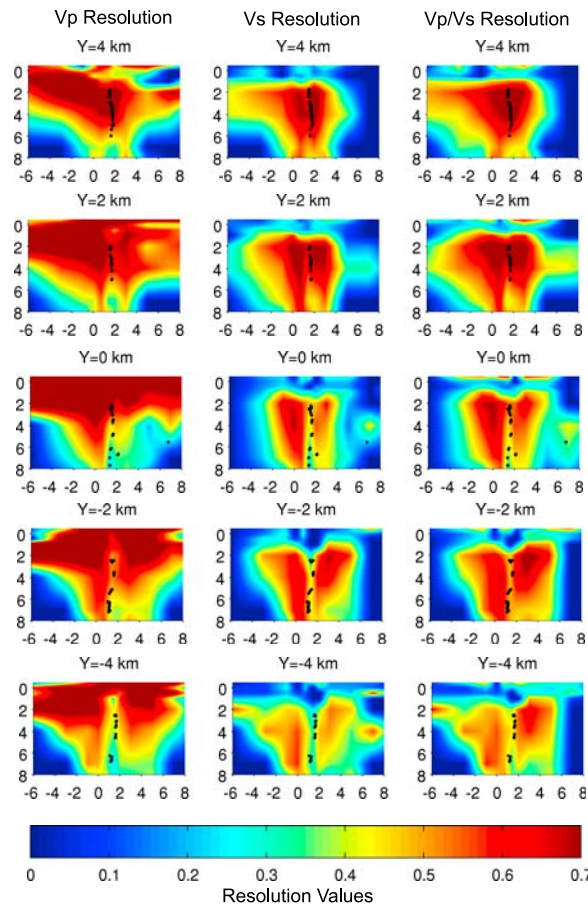


Figure 4. Diagonal resolution matrix values of Vp, Vs, and Vp/Vs for cross-fault cross sections at $Y = 4, 2, 0, -2$, and -4 km.

distribution. Based on the DWS and resolution distributions, the Vp, Vs, and Vp/Vs models are relatively well resolved in the range of $X = -3$ to 5 km, $Y = -4$ to 6 km and $Z = 1$ to 8 km.

5. Results and Discussion

[16] Across-fault cross sections of the Vp, Vs, and Vp/Vs models are shown in Figure 5. Horizontal slices of the Vp, Vs, and Vp/Vs models at depths of $1, 2, 4$ and 7 km are shown in Figure 6.

5.1. Vp and Vs Models

[17] As shown in previous tomography studies, the 3-D structure around Parkfield is dominated by the velocity contrast across the SAF, with the southwest side fast [Lees and Malin, 1990; Michelini and McEvilly, 1991; Eberhart-Phillips and Michael, 1993; Thurber et al., 2003, 2004; Zhang and Thurber, 2005] (Figures 5 and 6). In our Vp model, furthermore, there is a distinct low-

velocity zone (LVZ) along most of the SAF down to a depth of about 7 km (Figure 5), indicated by the V-shaped contours. A similar zone is seen in the Vs model for some cross sections (Figure 5). Most previous seismic tomography studies have not imaged this deep, relatively narrow zone. Exceptions are the joint seismic-gravity inversion model of Roecker et al. [2004] and one of four adaptive mesh tomography models of Zhang and Thurber [2005]. Li et al. [2004] and Li and Malin [2008] observed fault zone trapped waves recorded at both surface and borehole seismic sensors in the Parkfield area and, using waveform modeling, interpreted them as requiring an LVZ about 200 m wide extending to approximately 7 km depth, with a seismic velocity reduction of 25% to 40% compared to wall rock velocities. In our model, the velocity near the fault is reduced by only 10% to 20% compared to the surrounding velocities, and the LVZ is on the order of 1 km wide. The model resolution analysis shows that the Vp model is well resolved down to 7 km depth near the fault zone (Figure 4). The amplitudes of low-velocity anomaly

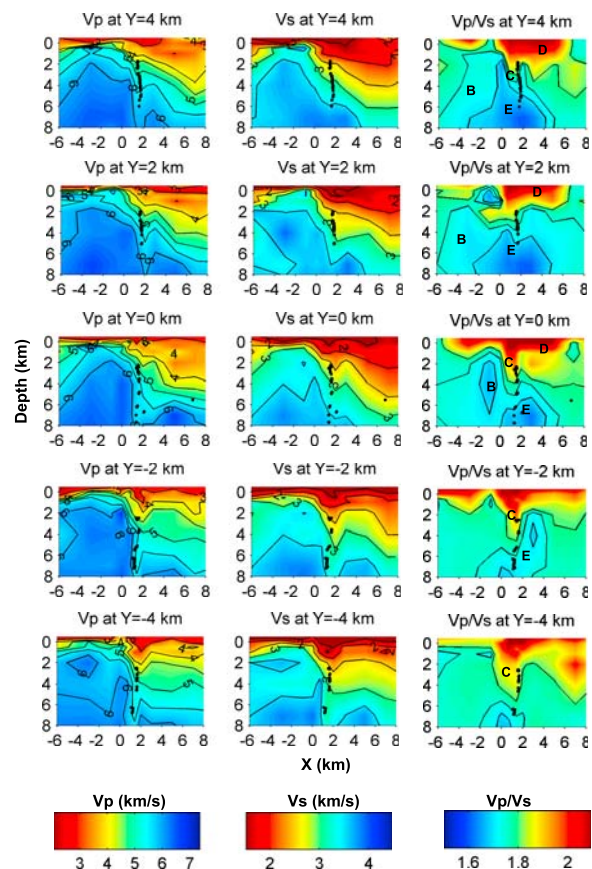


Figure 5. Across-fault cross sections of the Vp, Vs, and Vp/Vs models at $Y = 4, 2, 0, -2$, and -4 km. SAF is located around $X = 1.7$ km.

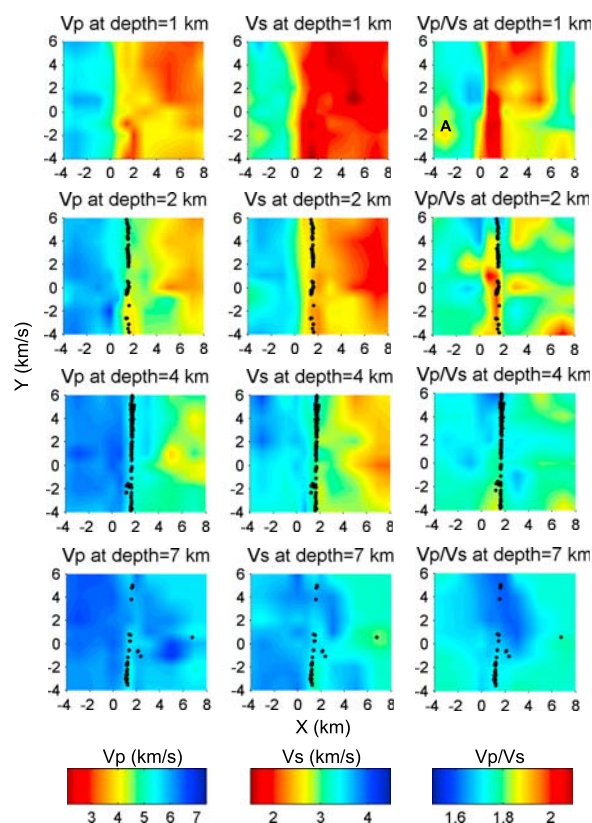


Figure 6. Horizontal slices of the Vp, Vs, and Vp/Vs models at depths of 1, 2, 4, and 7 km. SAF is located around $X = 1.7$ km.

lies are generally underestimated and are smeared spatially by seismic tomography [e.g., *Thurber and Ritsema, 2007*], so the true reduction could be greater and the zone width narrower than our models indicate.

5.2. Vp/Vs Model

[18] Previously, the most complete published Vp/Vs model around the SAFOD site was presented by *Thurber et al. [2003]*. They used P arrival times and S-P times from 453 local earthquakes and 6 explosions and the simul2000 algorithm [*Thurber and Eberhart-Phillips, 1999*] to determine earthquake locations and 3-D Vp and Vp/Vs structure. In the present study, we use a larger number of earthquakes and explosions and also include waveform cross-correlation data. As discussed above, the Vp, Vs, and Vp/Vs models were determined simultaneously using P, S, and S-P times. The enlarged data set and new inversion strategy jointly contribute to determining an improved Vp/Vs model around the SAFOD site.

[19] At shallow depths (-0.5 to 1 km) on the SW side of the fault, there is a high Vp/Vs anomaly

(>1.75) in the region from $X = -4$ to -2 km and $Y = -4$ to 2 km (marked by A in Figure 6). This high Vp/Vs anomaly corresponds to low Vp and Vs values (Figures 5 and 6) and also low Qp and Qs features found by *Bennington et al. [2008]*. It is attributed to Cenozoic sedimentary rocks that are thickening to the southwest [*Thurber et al., 2003; Hole et al., 2006*] (Figure 5). The underlying low Vp/Vs zone (~ 1.7 ; marked by B in Figure 5) corresponds well to high Vp and Vs values (Figure 5) and high Qp and Qs values [*Bennington et al., 2008*], interpreted to be the Salinian basement rocks.

[20] There is another high Vp/Vs zone just to the southwest of the SAF trace that is about 1 to 2 km wide (Figures 5 and 6; marked by C in Figure 5). The relocated earthquakes align directly along the northeast side of this high-Vp/Vs zone. Southeast of $Y = 2$ km, the zone extends as deep as 4 km, and it is somewhat shallower to the northwest. Compared to the geological cross section at SAFOD [*Bradbury et al., 2007*], this zone is coincident with a package of sedimentary rocks that abut the Salinian basement to the southwest and the SAF trace to the northeast. It also corresponds to an area with low Qp and Qs values (Figure 7).

[21] To the northeast of the SAF trace, the Vp/Vs values are again high at shallow depths (marked by D in Figure 5). They are correlated with low Vp, Vs, Qp, and Qs values and are generally consistent with the presence of fluids and low resistivities [*Jongmans and Malin, 1995; Unsworth et al., 1997, 2000*]. Around $X = -2$ to 4 km and at greater depths, the Vp/Vs values are lower, less than 1.7 (Figures 5 and 6; marked by E in Figure 5). They also correspond well to the high Qp and Qs values found by *Bennington et al. [2008]*, who interpreted this to be an area of Franciscan rocks. Our Vp/Vs results suggest instead that this may be a sliver of Salinian granitic rocks.

5.3. Comparing Vp, Vs, and Vp/Vs Values to Borehole Data

[22] We also compare our model to the borehole velocity logs in the main SAFOD hole (Figure 8) [*Zoback et al., 2005*]. We find that the Vp values extracted from our 3-D model are consistent with the log data. In contrast, the Vs and Vp/Vs values extracted from the inverted models are not as close to the log data as the estimated Vp values. For Vs, the model-estimated values are generally lower than the log data, although the overall patterns are similar. For Vp/Vs, the model-derived Vp/Vs

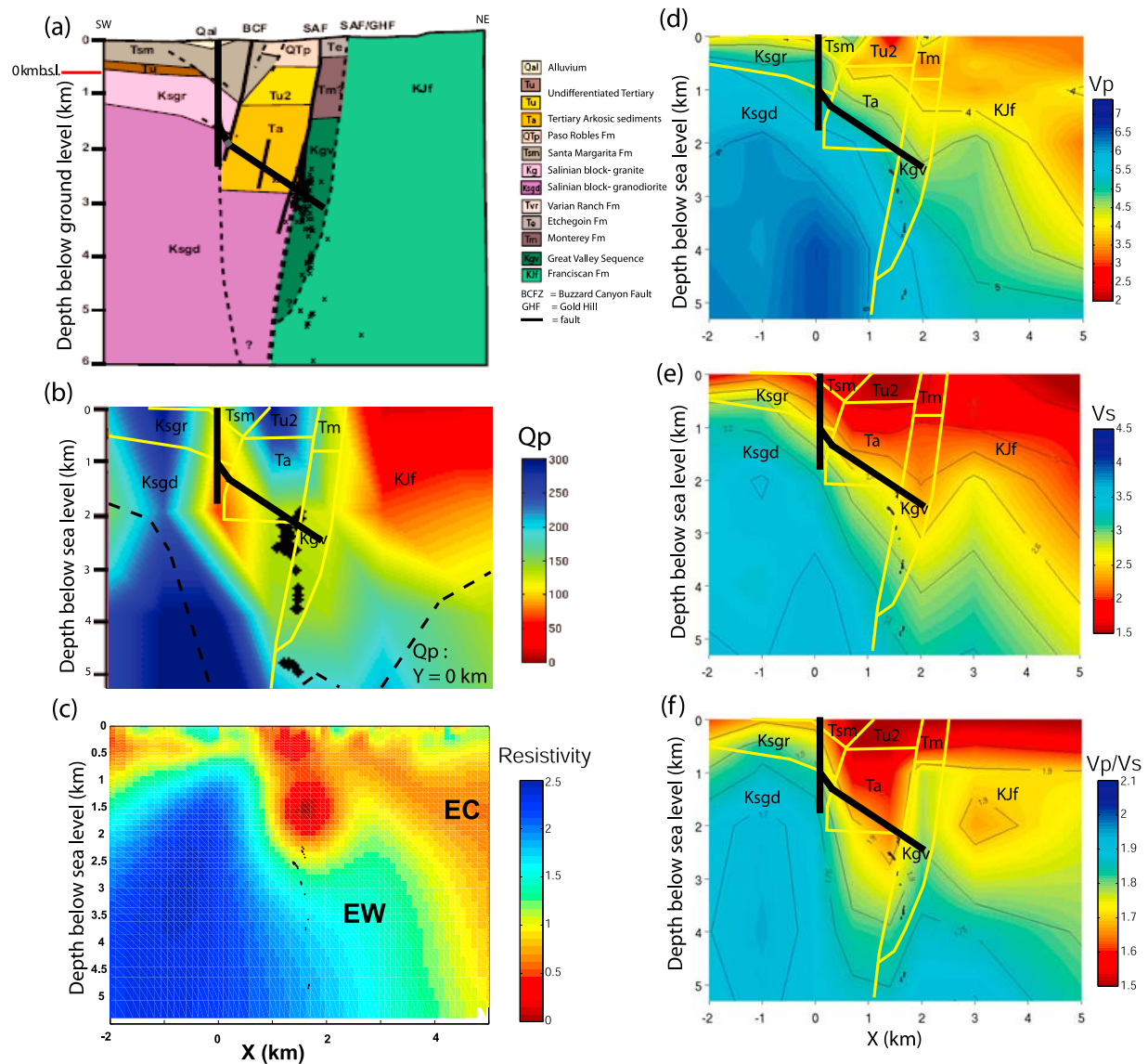


Figure 7. Across-fault cross sections of the geology [Bradbury *et al.*, 2007], V_p , V_p/V_s , Q_p [Bennington *et al.*, 2008], and resistivity [Unsworth and Bedrosian, 2004] models through the SAFOD site. Black thick lines are the SAFOD main and pilot boreholes. Yellow lines are delineated faults from Bradbury *et al.* [2007]. Black dots are relocated earthquakes.

values are generally higher than the log data. One cause for the relatively poor matching of V_s and V_p/V_s values is that we do not have S travel times from explosions to sensors in the borehole, therefore the spatial resolution for the V_s and V_p/V_s models is not as good as for the V_p model. Another potential cause for this discrepancy is anisotropy in the sedimentary rocks encountered at vertical depths greater than 2 km along the borehole [Boness and Zoback, 2006]. The sonic log measures the velocity along the borehole direction while seismic tomography gives an average velocity. Finally, it is possible that there were errors in the

shear velocity log and/or the tomography model because shear waves are more difficult to recognize and pick.

5.4. Comparing V_p , V_s , and V_p/V_s to the Resistivity Structure

[23] Many studies have shown significant correlations between electrical resistivity and seismic velocity structure, both theoretical [Schmeling, 1986; L. MacGregor, personal communication, 2007] and empirical at a variety of scales (borehole logs [Herwanger, 2001], cross-hole tomography

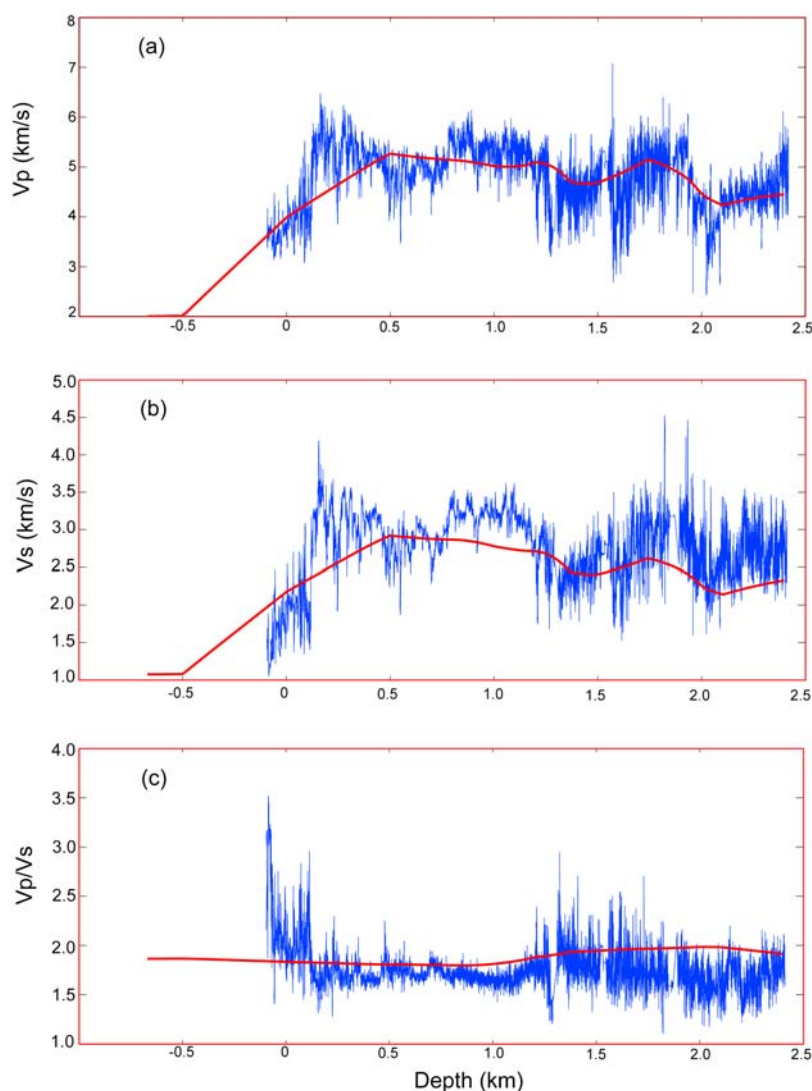


Figure 8. Comparison of the V_p , V_s , and V_p/V_s values along the SAFOD trajectory (red) to the borehole data (blue).

[Herwanger *et al.*, 2004; Saunders *et al.*, 2005], local crustal models [Eberhart-Phillips *et al.*, 1995], and crustal transects [Fujinawa *et al.*, 2002]. Unsworth *et al.* [1997, 2000] and Unsworth and Bedrosian [2004] have developed a high-resolution image of the resistivity structure near SAFOD using continuous MT profiling (Figure 7). First we make a qualitative comparison of the resistivity and seismic models and then present a quantitative correlation analysis and interpretation.

[24] On the northeast side of the SAF, the resistivity model has a deeply penetrating zone of low resistivity termed the Eastern Conductor (EC) by Unsworth and Bedrosian [2004] (Figure 7). They interpret it as a synclinal structure containing saline fluids, presumably within sediments of the

Great Valley Sequence. Between it and the seismicity defining the SAF at depth, there is a zone of increasing resistivity they term the East Wall (EW) of the SAF. Unsworth and Bedrosian [2004] suggest that the porosity in the EW is high enough (1–10% or greater) for this to be a pathway for fluids into the SAF at seismogenic depths. There are distinct differences, however, between the MT image of the EW and the structure of the corresponding region in the seismic model (Figure 7). In the area of the EW, the seismic model has P wave velocity values that are moderately high (approximately 5.5 km/s and above; Figure 7). In addition, Bennington *et al.* [2008] find that Q_p and Q_s are relatively high where the EW is located, implying that porosity is relatively low. Thus the seismic results do not support the

interpretation of the EW being a fluid pathway from the EC into the SAF at depth.

[25] The velocity and resistivity structures to the SW side of the SAF appear more consistent except in the upper 1–2 km. The MT results are likely better constrained than the seismic results at shallow depths except in the immediate vicinity of SAFOD. The seismic results near SAFOD, which include surface-to-borehole explosion data recorded in both the pilot and main holes, show a sharper transition from the Salinian granitic rocks on the SW to the lower-velocity fault zone rocks corresponding to the fault zone conductor (FZC). The Vp/Vs model has some features that are compatible with the Vp and/or resistivity models (Figures 5 and 7), but there are again apparent discrepancies, such as the deeper extension of the high Vp/Vs zone just NE of SAFOD compared to the FZC and the corresponding low Vp zone, a reversal in Vp/Vs near 2 km depth on the NE edge of the seismic model where the Vp and resistivity models show no major features, and a zone of surprisingly low Vp/Vs in the area of the EW in the resistivity model.

[26] In order to explore the joint interpretation of these models further, we present a quantitative correlation analysis between the seismic velocity models (Vp, Vs, and Vp/Vs) along our Y = 0 km section and the resistivity model of *Unsworth and Bedrosian* [2004], following the approach of *Bedrosian et al.* [2007]. Briefly, interpolation is used to produce a set of colocated model points, each identified with multiple physical properties and a unique subsurface location. Together with uncertainty estimates in the model parameters at each point, a probability density function (pdf) is assembled in the joint parameter space (JPS; e.g., Vp and $\log(\rho)$). Classes are subsequently identified as localized regions of enhanced probability density (specifically, points lying within 1 standard deviation of the 2-D Gaussian peaks fit to the pdf's) and then mapped back to the spatial domain (a depth section) where each class is interpreted as a distinct geologic structure (lithology). The classification approach has a number of advantages, including objective determination of lithologic boundaries, well-defined physical property ranges for identified structures, and realistic uncertainty estimates [*Bedrosian*, 2007].

[27] We acknowledge that there is no unambiguous way to divide up the JPS into a defined set of clusters or classes. If the physical property models (Vp, Vs, Vp/Vs, resistivity) perfectly represented

the subsurface structure and each distinct lithology had no variation in physical properties, then the JPS would be a series of points, one per lithology, each with a probability density of 1. In reality, the imperfect recovery of structure (data errors, model sensitivity, model regularization) together with natural variability in the physical properties of any given lithology lead to the “fuzzy” JPS images shown.

[28] The idea of using a threshold value fails in part because of the different spatial volumes associated with each lithology. Some class may show up prominently if it comprises a large part of the model sections. Unfortunately there is no way to a priori normalize for a cluster's spatial area while trying to determine the clusters themselves. In short, a thin layer will not produce as large a peak in the JPS as a thick layer.

[29] We are thus left with trying to define, as objectively as possible, the number of distinct classes and their boundaries. We furthermore strive to define nonoverlapping class boundaries so as not to end up with model points with multiple class membership. The approach we have taken, to do a parametric fit to the JPS surface as the sum of bivariate Gaussians, has several advantages. First, upon specifying the number of “classes” to be fit, we solve for a global fit to the JPS probability surface. Second, the resulting class boundaries, taken as full-width half maximum for each peak, have statistical meaning (68% confidence interval). Finally, we obtain a global misfit, which, when run for 2, 3, 4 ... N class models, allows us to assemble an L curve of misfit versus number of classes. From this it is usually possible to determine the optimal number of classes represented within the JPS surface.

[30] The pdf's and the spatial mapping of clusters for Vp, Vs, and Vp/Vs versus resistivity are shown in Figures 9 and 10, respectively. The Vp and Vs pdf plots (Figures 9a and 9b) have 5 peaks with a similar pattern, and the clusters in the JPS map back into connected regions in the spatial domain, which are similar for the Vp/ ρ and Vs/ ρ classifications (Figures 10a and 10b). The high Vp, Vs, and resistivity class shows up prominently because it comprises a large part of the model sections and is weighted accordingly. Some of the same clusters and spatial domains are evident in the Vp/Vs results as well (Figures 9c and 10c), but there are also significant differences. In addition, there are significant gaps between the spatial domains, indicating regions where the models do not show

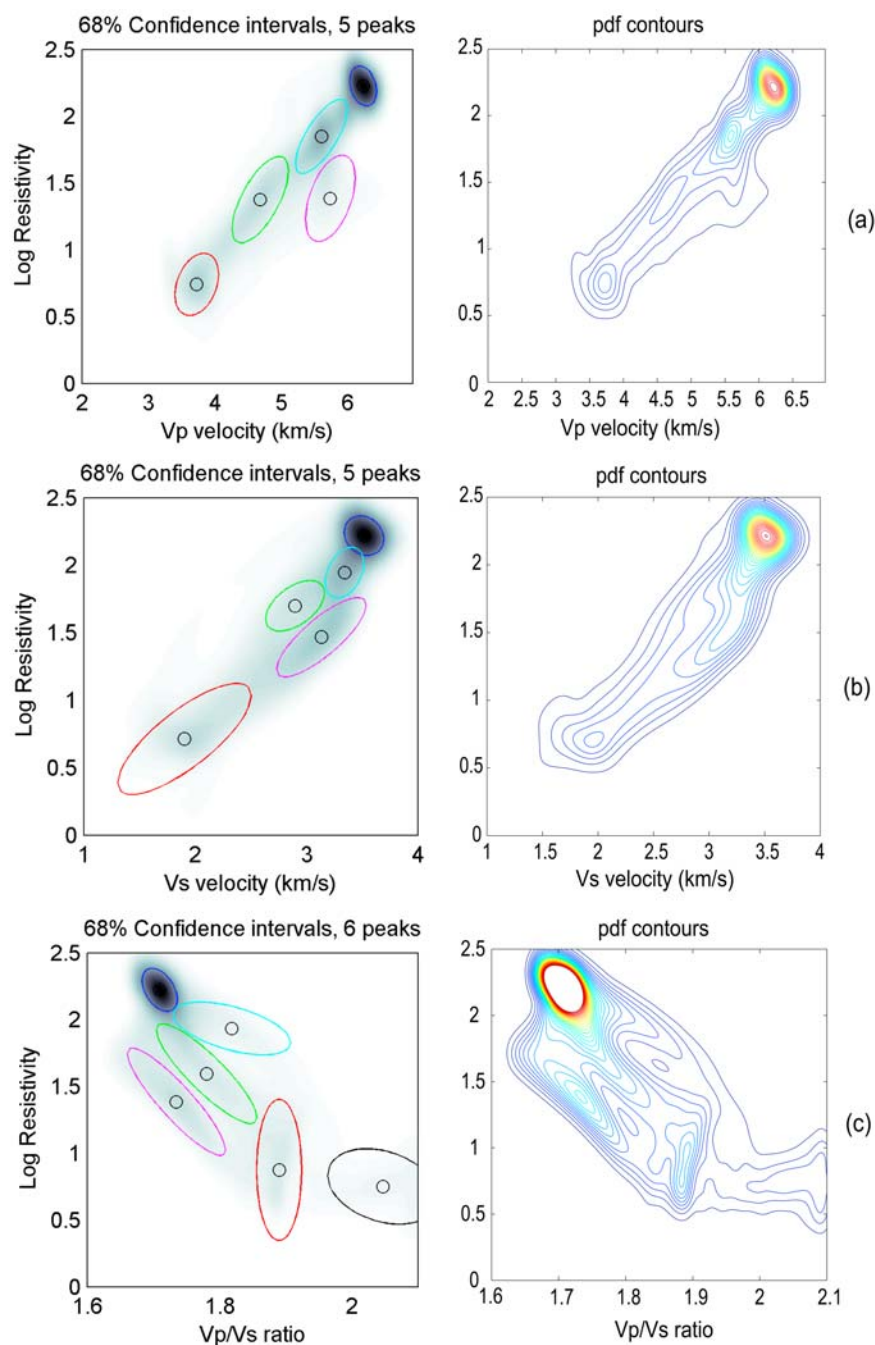


Figure 9. The pdf's and clusters for (a) Vp, (b) Vs, and (c) Vp/Vs versus resistivity. The contours are plotted for probability density values of 0 to 0.7 with an interval of 0.025.

strong correlation and/or the effect of blurring in the models, with points falling outside the 68% confidence intervals. These areas include the region of the granitic rocks penetrated by the SAFOD borehole (0 km horizontal distance, ~0 to 2 km depth).

[31] We propose the following interpretation of the clusters and domains based on the Vp and Vs

classification results, recognizing that the boundaries are not precisely determined: red, fluid-rich sedimentary rocks of the Great Valley Sequence (GVS); green, fractured Franciscan rocks and/or GVS sediments more highly compacted and with lower fluid content than the above red class (to the SW of the fault, Santa Margarita Formation); cyan, Franciscan rocks to the NE of the fault; weathered granite to the SW of the fault; purple, intact gran-

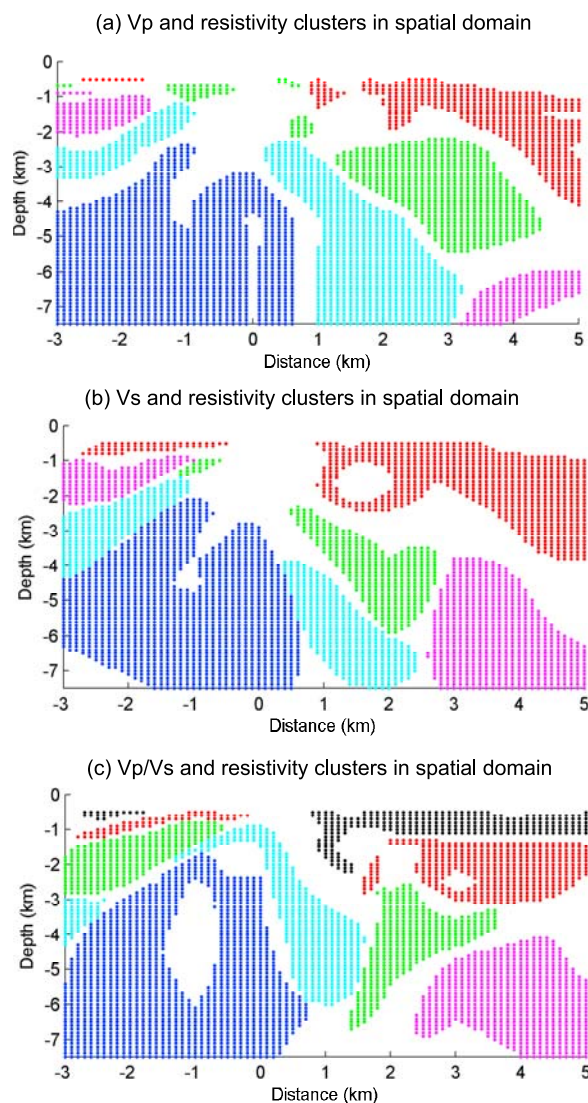


Figure 10. The spatial mapping of clusters for (a) V_p , (b) V_s , and (c) V_p/V_s versus resistivity.

odiorites (west wall country rock); and magenta, Franciscan rocks largely undeformed by present-day tectonics (east wall country rock) (to the SW of the fault may represent weathered granite).

[32] The red cluster has very low V_p (<4.0 km/s) and V_s (<2.5 km/s), moderately high V_p/V_s (~ 1.9), very low resistivity (<10 Ohm m), and maps primarily to near-surface rocks to the NE of the SAF. This cluster represents shallow Tertiary sedimentary rocks to the NE of the SAF [e.g., *McPhee et al.*, 2004], although Franciscan rocks likely exist here as well. The green cluster has moderately low V_p (~ 4.5 to 5.0 km/s), intermediate V_s (~ 3 km/s), moderately low resistivity (~ 30 to 50 Ohm m), and corresponds mainly to a zone between 2 and 5 km depth on the NE side of the

SAF. From a geologic perspective, these are most likely Franciscan rocks, but with lower velocities than typical Franciscan rocks [e.g., *Brocher*, 2005], suggesting they are somewhat fractured and/or overpressured. Alternatively, *McPhee et al.* [2004] hypothesize the presence of serpentinite here at ~ 2 to 4 km depth to account for an observed magnetic high and the low-velocity structure. Other parts of the green domain in the near-surface southwest of the SAF are interpreted as high-velocity sedimentary rocks of the Tertiary Santa Margarita Formation, similar to those encountered at depth in the SAFOD borehole [*Hickman et al.*, 2004]. The cyan cluster has moderately high V_p (~ 5.5 km/s) and V_s (~ 3.2 km/s) and somewhat higher resistivity (70 to 120 Ohm m). These parameters are generally consistent with either Franciscan rocks or fractured/weathered granite; however, the poorly defined V_p/V_s cluster prevents a clear discrimination. The purple cluster, on the other hand, has very high V_p (>6 km/s) and V_s (>3.4 km/s), a relatively low V_p/V_s (<1.7), and high resistivity (~ 175 Ohm m). Given the spatial location of its domain at depth on the SW side of the SAF, together with available geologic information, we are confident in interpreting this as the granodiorites comprising the basement of the Salinian block. The magenta cluster, primarily confined to the NE side of the SAF at depths greater than 4 km is most likely Franciscan rocks largely unaffected by the present-day tectonics along the SAF margin. The zone of magenta between 1 and 2 km depth on the SW side of the fault may represent weathered granite of the Salinian block. Finally, from the V_p/V_s plots (Figures 9c and 10c), we interpret the black cluster as representing fluid-enriched sediments, based on their very low resistivity and high V_p/V_s ratio.

5.5. Earthquake Locations, Velocity, and Resistivity Structure

[33] The relationship between the seismicity and velocity structure is quite striking. Areas with $V_p/V_s > 1.93$, which are limited here to depths shallower than 3 km, are virtually devoid of earthquakes (Figures 5 and 11). Similar observations have been reported previously for the Loma Prieta and Hollister sections of the SAF [*Thurber et al.*, 1995, 1997]. We also find that seismicity is completely restricted to areas with $V_p > 3.4$ km/s and $V_s > 1.9$ km/s, with 99% of the hypocenters corresponding to areas with $V_p > 3.5$ km/s and $V_s > 2.0$ km/s (Figure 11). This is below the 4.5 km/s value *Thurber et al.* [2007] found for the

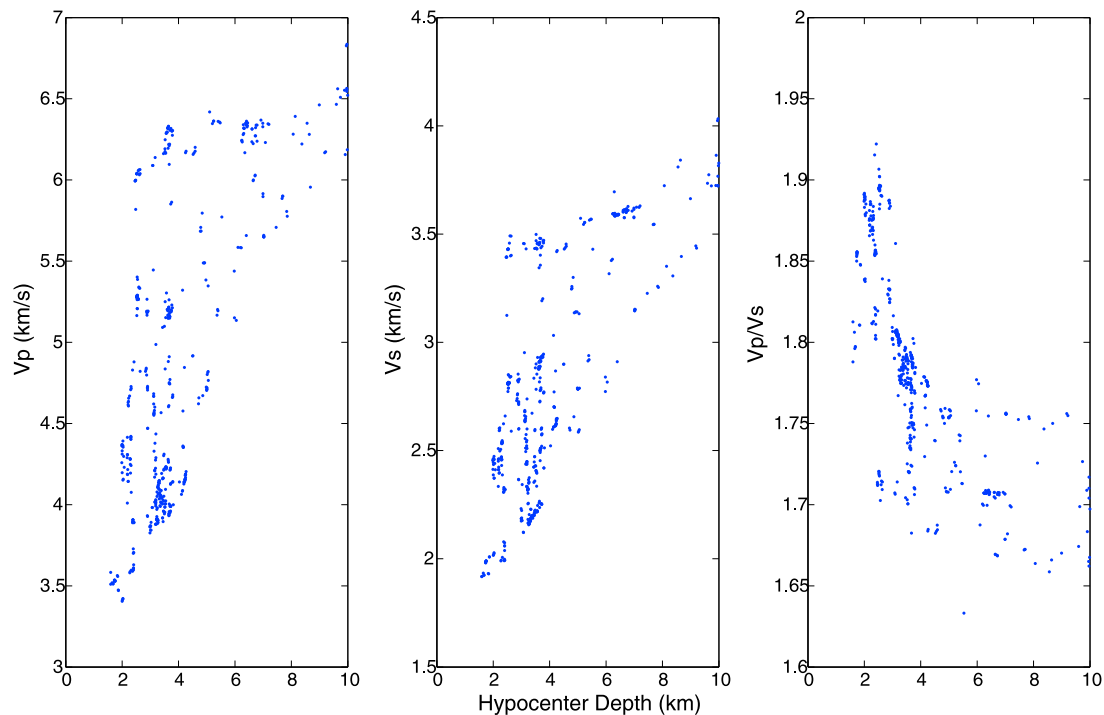


Figure 11. Scatterplot of hypocenter depth versus V_p , V_s , and V_p/V_s at the hypocenter.

99% percentile of earthquakes in the greater San Francisco Bay area, but their events extended only down to magnitude 2 compared to magnitude ~ 0 and above in our study. We also note that this area was selected for SAFOD in part because of the presence of unusually shallow magnitude ~ 2 earthquakes.

[34] Seismicity and resistivity show a strong spatial correlation as well, with strong conductive regions almost devoid of seismicity. The onset of seismicity, as seen in Figure 7, corresponds closely with a strong increase in resistivity around 2 km depth. This correlation has been noted further north along the SAF [Bedrosian *et al.*, 2004] and has been attributed to decreased mechanical strength within areas of high fluid content, thus prohibiting the buildup of shear stress necessary for brittle failure. Thus, a combination of high fluid content, extensive fracturing, and/or insufficient lithification is sufficient to suppress the occurrence of earthquakes at shallow depths down to magnitude 0 in this region.

6. Conclusions

[35] We have developed new 3-D V_p , V_s , and V_p/V_s models around the SAFOD site using a new DD

tomography code tomoDDPS, which solves simultaneously for V_p , V_s , and V_p/V_s , and event locations using both absolute and differential times. This approach avoids the issue of resolution bias affecting the evaluation of V_p/V_s by dividing V_p by V_s (or V_s by dividing V_p by V_p/V_s) [Eberhart-Phillips, 1990; Wagner *et al.*, 2005]. The 3-D structure around SAFOD is dominated by a strong velocity contrast across the SAF, which has been imaged in many previous tomography studies. We also imaged a clear LVZ along the SAF that penetrates as deep as 7 km, which has a width and velocity contrast that is compatible with the LVZ found using fault zone trapped waves [Li and Malin, 2008] when resolution differences are considered. Shallow zones of high V_p/V_s correlate with areas of sediments and/or inferred fracturing and high fluid content. A zone of strong low V_p/V_s at depth southwest of the SAF corresponds to Salinian basement rock. A correlation analysis between the seismic velocity models and a resistivity model along a section through SAFOD leads to five primary clusters that are interpreted in terms of lithology, fracturing, and fluid content. Finally, we find a strong correlation between V_p value and the presence or absence of seismicity: areas with V_p below 3.4 km/s are devoid of earthquakes down to magnitude ~ 0 .

Acknowledgments

[36] This material is based upon work supported by the National Science Foundation under grants EAR-0346105 and EAR-0454511. Research is also supported in part by the Department of Energy/NNSA under contract DE-FC52-06NA27325; the content does not necessarily reflect the position or policy of the U.S. government, and no official endorsement should be inferred. We are grateful for the constructive comments from Darcy McPhee and Karl Ellefsen of U.S. Geological Survey, Associated Editor Thorsten Becker, and two anonymous reviewers. We also thank Ninfa Bennington for her help on preparing Figures 1 and 7. The instruments used in the field program were provided by the PASSCAL facility of the Incorporated Research Institutions for Seismology (IRIS) through the PASSCAL Instrument Center at New Mexico Tech. Data collected during this experiment are available through the IRIS Data Management Center. The facilities of the IRIS Consortium are supported by the National Science Foundation under cooperative agreement EAR-0552316.

References

- Abercrombie, R. (2000), Crustal attenuation and site effects at Parkfield, California, *J. Geophys. Res.*, *105*, 6277–6286, doi:10.1029/1999JB900425.
- Becken, M., O. Ritter, S. K. Park, P. A. Bedrosian, U. Weckmann, and M. Weber (2008), A deep crustal fluid channel into the San Andreas Fault system near Parkfield, California, *Geophys. J. Int.*, *173*, 718–732, doi:10.1111/j.1365-246X.2008.03754.x.
- Bedrosian, P. A. (2007), MT+, integrating magnetotellurics to determine earth structure, physical state, and processes, *Surv. Geophys.*, *28*, 121–167, doi:10.1007/s10712-007-9019-6.
- Bedrosian, P., M. Unsworth, G. Egbert, and C. Thurber (2004), Geophysical images of the creeping segment of the San Andreas fault: Implications for the role of crustal fluids in the earthquake process, *Tectonophysics*, *385*, 137–158, doi:10.1016/j.tecto.2004.02.010.
- Bedrosian, P. A., N. Maercklin, U. Weckmann, Y. Bartov, T. Ryberg, and O. Ritter (2007), Lithology-derived structure classification from the joint interpretation of magnetotelluric and seismic models, *Geophys. J. Int.*, *170*(2), 737–748, doi:10.1111/j.1365-246X.2007.03440.x.
- Bennington, N., C. Thurber, and S. Roecker (2008), Three-dimensional seismic attenuation structure around the SAFOD site, Parkfield, California, *Bull. Seismol. Soc. Am.*, *98*, 2934–2947, doi:10.1785/0120080175.
- Ben-Zion, Y., and P. Malin (1991), San Andreas fault zone head waves near Parkfield, California, *Science*, *251*, 1592–1594, doi:10.1126/science.251.5001.1592.
- Bleibinhaus, F., J. A. Hole, T. Ryberg, and G. S. Fuis (2007), Structure of the California Coast Ranges and San Andreas Fault at SAFOD from seismic waveform inversion and reflection imaging, *J. Geophys. Res.*, *112*, B06315, doi:10.1029/2006JB004611.
- Boness, N., and M. Zoback (2006), A multiscale study of the mechanism controlling shear velocity anisotropy in the San Andreas Fault Observatory at Depth, *Geophysics*, *71*(5), F131–F146, doi:10.1190/1.2231107.
- Bradbury, K. K., D. C. Barton, J. G. Solum, S. D. Draper, and J. P. Evans (2007), Mineralogical and textural analyses of drill cuttings from the San Andreas Fault Observatory at Depth (SAFOD) boreholes: Initial interpretations of fault zone composition and constraints on geologic models, *Geosphere*, *3*, 299–318, doi:10.1130/GES00076.1.
- Brocher, T. M. (2005), Empirical relations between elastic wavespeeds and density in the Earth's crust, *Bull. Seismol. Soc. Am.*, *95*, 2081–2092, doi:10.1785/0120050077.
- Catchings, R. D., M. J. Rymer, M. R. Goldman, J. A. Hole, R. Huggins, and C. Lippus (2002), High-resolution seismic velocities and shallow structure of the San Andreas Fault Zone at Middle Mountain, Parkfield, California, *Bull. Seismol. Soc. Am.*, *92*, 2493–2503, doi:10.1785/0120010263.
- Chavarria, J. A., P. Malin, R. D. Catchings, and E. Shalev (2003), A look inside the San Andreas fault at Parkfield through vertical seismic profiling, *Science*, *302*, 1746–1748, doi:10.1126/science.1090711.
- Christensen, N. (1996), Poisson's ratio and crustal seismology, *J. Geophys. Res.*, *101*(B2), 3139–3156, doi:10.1029/95JB03446.
- Du, W.-X., C. H. Thurber, and D. Eberhart-Phillips (2004), Earthquake relocation using cross-correlation time delay estimates verified with the bispectrum method, *Bull. Seismol. Soc. Am.*, *94*, 856–866, doi:10.1785/0120030084.
- Eberhart-Phillips, D. (1990), Three-dimensional P and S velocity structure in the Coalinga region, California, *J. Geophys. Res.*, *95*, 15,343–15,363, doi:10.1029/JB095iB10p15343.
- Eberhart-Phillips, D., and A. J. Michael (1993), Three-dimensional velocity structure, seismicity, and fault structure in the Parkfield region, central CA, *J. Geophys. Res.*, *98*, 15,737–15,758, doi:10.1029/93JB01029.
- Eberhart-Phillips, D., W. D. Stanley, B. D. Rodriguez, and W. J. Lutter (1995), Surface seismic and electrical methods to detect fluids related to faulting, *J. Geophys. Res.*, *100*, 12,919–12,936, doi:10.1029/94JB03256.
- Fisher, N. I. (1995), *Statistical Analysis of Circular Data*, 277 pp., Cambridge Univ. Press, New York.
- Fujinawa, Y., N. Kawakami, J. Inoue, T. H. Asch, and S. Takasugi (2002), Conductivity distribution and seismicity in the northeastern Japan Arc, *Earth Planets Space*, *54*, 629–636.
- Herwanger, J. V. (2001), Seismic and electric crosshole tomography for fracture detection and characterization, Ph.D. thesis, Imperial Coll. of Sci., London.
- Herwanger, J. V., M. H. Worthington, R. Lubbe, A. Binley, and J. Khazanehdari (2004), A comparison of crosshole electrical and seismic data in fractured rock, *Geophys. Prospect.*, *52*, 109–121, doi:10.1046/j.1365-2478.2003.00402.x.
- Hickman, S., M. Zoback, and W. Ellsworth (2004), Introduction to special section: Preparing for the San Andreas Fault Observatory at Depth, *Geophys. Res. Lett.*, *31*, L12S01, doi:10.1029/2004GL020688.
- Hole, J. A., R. D. Catchings, K. C. St. Clair, M. J. Rymer, D. A. Okaya, and B. J. Carney (2001), Steep-dip imaging of the shallow San Andreas fault near Parkfield, *Science*, *294*, 1513–1515, doi:10.1126/science.1065100.
- Hole, J., T. Ryberg, G. Fuis, F. Bleibinhaus, and A. Sharma (2006), Structure of the San Andreas fault zone at SAFOD from a seismic refraction survey, *Geophys. Res. Lett.*, *33*, L07312, doi:10.1029/2005GL025194.
- Jongmans, D., and P. Malin (1995), Vertical profiling of micro-earthquake S waves in the Varian well at Parkfield, California, *Bull. Seismol. Soc. Am.*, *85*, 1805–1820.
- Koch, M. (1992), Bootstrap inversion for vertical and lateral variations of the S wave structure and the V_p/V_s -ratio from shallow earthquakes in the Rhinegraben seismic zone,

- Germany, *Tectonophysics*, 210, 91–115, doi:10.1016/0040-1951(92)90130-X.
- Larsen, R. M. (1998), Lanczos bidiagonalization with partial reorthogonalization, *Tech. Rep., DAIMI PB-357*, Dep. of Comput. Sci., Aarhus Univ., Aarhus, Denmark.
- Lees, J. M., and P. E. Malin (1990), Tomographic images of P wave velocity variation at Parkfield, California, *J. Geophys. Res.*, 95, 21,793–21,804, doi:10.1029/JB095iB13p21793.
- Li, Y.-G., and P. E. Malin (2008), San Andreas Fault damage at SAFOD viewed with fault-guided waves, *Geophys. Res. Lett.*, 35, L08304, doi:10.1029/2007GL032924.
- Li, Y.-G., W. L. Ellsworth, C. H. Thurber, P. Malin, and K. Aki (1997), Fault zone guided waves from explosions in the San Andreas fault at Parkfield and Cienega Valley, California, *Bull. Seismol. Soc. Am.*, 87, 210–221.
- Li, Y.-G., J. E. Vidale, and E. S. Cochran (2004), Low-velocity damaged structure of the San Andreas Fault at Parkfield from fault zone trapped waves, *Geophys. Res. Lett.*, 31, L12S06, doi:10.1029/2003GL019044.
- Liu, Y., H. Zhang, C. Thurber, and S. Roecker (2008), Shear wave anisotropy in the crust around the San Andreas fault near Parkfield: Spatial and temporal analysis, *Geophys. J. Int.*, 172, 957–970, doi:10.1111/j.1365-246X.2007.03618.x.
- Malin, P., E. Shalev, H. Balven, and C. Lewis-Kenedi (2006), Structure of the San Andreas Fault at SAFOD from P wave tomography and fault-guided wave mapping, *Geophys. Res. Lett.*, 33, L13314, doi:10.1029/2006GL025973.
- McPhee, D., R. Jachens, and C. Wentworth (2004), Crustal structure across the San Andreas Fault at the SAFOD site from potential field and geologic studies, *Geophys. Res. Lett.*, 31, L12S03, doi:10.1029/2003GL019363.
- Michellini, A., and T. V. McEvelly (1991), Seismological studies at Parkfield. I. Simultaneous inversion for velocity structure and hypocenters using cubic B-splines parameterization, *Bull. Seismol. Soc. Am.*, 81, 524–552.
- Page, B. M. (1981), The southern Coast Ranges, in *The Geotectonic Development of California*, edited by W. G. Ernst, pp. 329–417, Prentice-Hall, Upper Saddle River, N. J.
- Roecker, S., C. Thurber, and D. McPhee (2004), Joint inversion of gravity and arrival time data from Parkfield: New constraints on structure and hypocenter locations near the SAFOD drill site, *Geophys. Res. Lett.*, 31, L12S04, doi:10.1029/2003GL019396.
- Roecker, S., C. Thurber, K. Roberts, and L. Powell (2006), Refining the image of the San Andreas Fault near Parkfield, California using a finite difference travel time computation technique, *Tectonophysics*, 426, 189–205, doi:10.1016/j.tecto.2006.02.026.
- Saunders, J. H., J. V. Herwanger, C. C. Pain, M. H. Worthington, and C. R. E. de Oliveira (2005), Constrained resistivity inversion using seismic data, *Geophys. J. Int.*, 160, 785–796, doi:10.1111/j.1365-246X.2005.02566.x.
- Schmeling, H. (1986), Numerical models on the influence of partial melt on elastic, anelastic, and electrical properties of rocks. Part II: Electrical conductivity, *Phys. Earth Planet. Inter.*, 43, 123–136, doi:10.1016/0031-9201(86)90080-4.
- Thurber, C. H. (1993), Local earthquake tomography: Velocities and Vp/Vs theory, in *Seismic Tomography: Theory and Practice*, edited by H. M. Iyer and K. Hirahara, pp. 563–583, Chapman and Hall, New York.
- Thurber, C., and D. Eberhart-Phillips (1999), Local earthquake tomography with flexible gridding, *Comput. Geosci.*, 25, 809–818, doi:10.1016/S0098-3004(99)00007-2.
- Thurber, C., and J. Ritsema (2007), Theory and observations—Seismic tomography and inverse methods, in *Seismology and the Structure of the Earth, Treatise on Geophysics*, vol. 1, edited by G. Schubert, pp. 323–360, Elsevier, Amsterdam.
- Thurber, C. H., S. R. Atre, and D. Eberhart-Phillips (1995), Three-dimensional Vp and Vp/Vs structure at Loma Prieta, California, from local earthquake tomography, *Geophys. Res. Lett.*, 22(22), 3079–3082, doi:10.1029/95GL03077.
- Thurber, C., S. Roecker, W. Ellsworth, Y. Chen, W. Lutter, and R. Sessions (1997), Two-dimensional seismic image of the San Andreas fault in the northern Gabilan range, central California: Evidence for fluids in the fault zone, *Geophys. Res. Lett.*, 24, 1591–1594, doi:10.1029/97GL01435.
- Thurber, C., S. Roecker, K. Roberts, M. Gold, L. Powell, and K. Rittger (2003), Earthquake locations and three-dimensional fault zone structure along the creeping section of the San Andreas fault near Parkfield, CA: Preparing for SAFOD, *Geophys. Res. Lett.*, 30(3), 1112, doi:10.1029/2002GL016004.
- Thurber, C., S. Roecker, H. Zhang, S. Baher, and W. Ellsworth (2004), Fine-scale structure of the San Andreas fault zone and location of the SAFOD target earthquakes, *Geophys. Res. Lett.*, 31, L12S02, doi:10.1029/2003GL019398.
- Thurber, C., H. Zhang, F. Waldhauser, J. Hardebeck, A. Michael, and D. Eberhart-Phillips (2006), Three-dimensional compressional wavespeed model, earthquake relocations, and focal mechanisms for the Parkfield, California, region, *Bull. Seismol. Soc. Am.*, 96, S38–S49, doi:10.1785/0120050825.
- Thurber, C. H., T. M. Brocher, H. Zhang, and V. E. Langenheim (2007), Three-dimensional P wave velocity model for the San Francisco Bay region, California, *J. Geophys. Res.*, 112, B07313, doi:10.1029/2006JB004682.
- Toomey, D. R., and G. R. Foulger (1989), Tomographic inversion of local earthquake data from the Hengill-Grensdaalur central volcano complex, Iceland, *J. Geophys. Res.*, 94, 17,497–17,510, doi:10.1029/JB094iB12p17497.
- Unsworth, M., and P. Bedrosian (2004), Electrical resistivity at the SAFOD site from magnetotelluric exploration, *Geophys. Res. Lett.*, 31, L12S05, doi:10.1029/2003GL019405.
- Unsworth, M. J., P. E. Malin, G. D. Egbert, and J. R. Booker (1997), Internal structure of the San Andreas fault zone at Parkfield, *Calif. Geol.*, 25, 359–362.
- Unsworth, M., P. Bedrosian, M. Eisel, G. Egbert, and W. Siripunvaraporn (2000), Along strike variations in the electrical structure of the San Andreas Fault at Parkfield, California, *Geophys. Res. Lett.*, 27, 3021–3024, doi:10.1029/2000GL011476.
- Wagner, L. S., S. Beck, and G. Zandt (2005), Upper mantle structure in the south central Chilean subduction zone (30° to 36°S), *J. Geophys. Res.*, 110, B01308, doi:10.1029/2004JB003238.
- Walck, M. C. (1988), Three-dimensional Vp/Vs variations for the Coso region, California, *J. Geophys. Res.*, 93, 2047–2051, doi:10.1029/JB093iB03p2047.
- Zhang, H. (2003), Double-difference seismic tomography method and its applications, Ph.D. thesis, Univ. of Wis.–Madison, Madison.
- Zhang, H., and C. H. Thurber (2003), Double-difference tomography: The method and its application to the Hayward Fault, California, *Bull. Seismol. Soc. Am.*, 93, 1875–1889, doi:10.1785/0120020190.
- Zhang, H., and C. Thurber (2005), Adaptive mesh seismic tomography based on tetrahedral and Voronoi diagrams: Application to Parkfield, California, *J. Geophys. Res.*, 110, B04303, doi:10.1029/2004JB003186.
- Zhang, H., and C. H. Thurber (2007), Estimating the model resolution matrix for large seismic tomography problems based on Lanczos bidiagonalization with partial reorthogon-

- nalization, *Geophys. J. Int.*, *170*, 337–345, doi:10.1111/j.1365-246X.2007.03418.x.
- Zhang, H., Y. Liu, C. Thurber, and S. Roecker (2007), Three-dimensional shear-wave splitting tomography in the Parkfield, California, region, *Geophys. Res. Lett.*, *34*, L24308, doi:10.1029/2007GL031951.
- Zoback, M. D., S. Hickman, and W. Ellsworth (2005), Overview of SAFOD Phases 1 and 2: Drilling, sampling and measurements in the San Andreas Fault zone at seismogenic depth, *Eos Trans. AGU*, *86*(52), Fall Meet. Suppl., Abstract T23E-01.
- Zoback, M. D., S. H. Hickman, W. Ellsworth, D. Kirschner, N. B. Pennell, J. Chery, and S. Sobolev (2007), Preliminary results from SAFOD Phase 3: Implications for the state of stress and shear localization in and near the San Andreas Fault at depth in central California, *Eos Trans. AGU*, *88*(52), Fall Meet. Suppl., Abstract T13G-03.